RAS Techniques and Instruments

RASTAI **4,** 1–10 (2025) https://doi.org/10.1093/rasti/rzaf003
Advance Access publication 2025 February 12

Generating electron density archives using mainland EISCAT data between 2001 and 2021 at 10 min and 1 h integration

Jade A. Reidy,[1]★ A. J. Kavanagh,[1] I. Häggström,[2] D. R. Themens[3] and M. Wild[4]

[1]*British Anatarctic Survey, Cambridge, CB3 0ET, UK*
[2]*EISCAT Scientific Association, SE-981 92 Kiruna, Sweden*
[3]*Space Environment and Radio Engineering Group, School of Engineering, University of Birmingham, Birmingham, B15 2TT, UK*
[4]*Rutherford Appleton Laboratory, Harwell Campus, Didcot, OX11 0QX, UK*

Accepted 2025 January 8. Received 2024 December 13; in original form 2024 August 5

ABSTRACT

The mesosphere/lower thermosphere/ionosphere (MLTI) region is a critical boundary in the coupling of the atmosphere, climate, and space weather, however it is one of the least understood regions, making it hard to include in whole atmosphere models. The EISCAT radars at Tromsø, Norway (UHF and VHF) have been measuring ionospheric parameters, such as electron density, since 1985 making it an excellent resource to study changes in the ionosphere over a long time period. This paper details how we have combined high elevation data from both radars between 2001 and 2021, re-integrated at 10 min and 1 h, to look at the different sources of variability in the MLTI region between 50 and 200 km. Day of year climatology's of the electron density highlight that the VHF data are more prone to contamination from Polar Mesospheric summer Echos. The magnetic local time variation of the electron density shows seasonal and altitude dependence related to solar UV illumination and electron precipitation, as expected. We compare our archives to the Empirical Canadian High Arctic Ionospheric Model (E-CHAIM) and find the biggest differences during the winter months and below 100 km, where the model does not yet include the impact of high energy electron precipitation.

Key words: EISCAT – Instrumentation – Mesosphere – Ionosphere – Data archive.

Forecasting the behaviour of the whole atmosphere, both the neutral and the ionized parts, is a challenge due to the complex, coupled nature of the different regions (Akmaev 2011; Gimeno 2013). The mesosphere – lower thermosphere (60–120 km), overlaps with the Earth's ionosphere, the ionized layer of the Earth's atmosphere, and is therefore an important region in the atmosphere, coupling space weather and lower atmospheric effects. Historically, the Mesosphere, Lower Thermosphere-Ionosphere (MLT-I) region has been poorly constrained in models due to a lack of observations; however, over the last decade, more data have become available from both ground-based and satellite instrumentation, revealing the MLT-I region to be highly variable. This paper will outline a long-term data set from incoherent scatter radars capturing key measurements of the high latitude MLT-I region; these data sets were created with the aim to provide pathways to accurately constrain this region in whole atmospheric models.

The MLT-I region influences, and is influenced by, in-situ and external forces such as space weather effects (downward) and atmospheric waves and tides (upwards). The mesosphere is strongly coupled to the lower edge of the ionosphere, as well as the stratosphere and troposphere, so changes in one part of the atmosphere can impact on others.

The F-region ionosphere (150–500 km) is primarily produced by ionization from EUV solar radiation, which is variable on different time-scales, such as the 11-yr solar cycle, and regional location. At lower altitudes (<150 km), the E and D-region ionosphere (which overlap the mesosphere and lower thermosphere), particle precipitation becomes important. Particle precipitation is a particular feature of the high latitude ionosphere, where particles from the magnetosphere are funnelled by the Earth's magnetic field lines into the atmosphere, colliding with atmospheric particles. The source population of the precipitation is dependent on magnetic local time, with precipitation related to wave-particle interactions in the radiation belts typically peaking in the dawn-sector (Lam et al. 2010) and precipitation related to substorms, a major re-orientation in the Earth's magnetic field, typically peaking around magnetic midnight (Kavanagh et al. 2004, 2012) (plasma sheet particles also contribute on the dawnside). How far into the atmosphere a particle penetrates is dependent on its energy and mass, with the highest energy particles (>1 MeV) originating in the radiation belts penetrating as low as 50–60 km and auroral electrons (∼10 s keV) reaching around 100 km.

Lower atmospheric processes have been shown to influence ionospheric variability; Laštovička (2006) reviewed the importance of upward propagating waves on ionospheric variability, in particular the effects of tides, planetary waves, and gravity waves which can significantly modulate the ionospheric layers and their formation, particularly in the E-region. Pedatella & Liu (2018) demonstrated the importance of including lower atmospheric variability in modelling the ionospheric response to a geomagnetic storm, finding that omitting this factor led to 20–40 per cent uncertainty in the ionospheric response, which could go up to 100 per cent regionally.

★ E-mail: jadeid70@bas.ac.uk

Variations in ionospheric parameters, such as ion temperature, have been associated with sudden stratospheric warmings (SSWs) (e.g. Goncharenko & Zhang 2008). Goncharenko et al. (2010) even showed during periods of strong lower atmospheric forcing, such as major SSW events, this forcing can be of comparable magnitudes to forcing due to geomagnetic storms.

In this paper, we present two new archives of electron density generated from data taken by the European Incoherent Scatter (EISCAT) radars between 2001 and 2021 at 10 min and 1 h integration time. As discussed above, the variability of the MLT-I region is driven by a range of internal and external processes which are occurring on multiple time-scales, for example geomagnetic substorms which can last hours to daily atmospheric tides. These archives will provide us with the tools to determine the variability of the MLT-I region, and its drivers, over a subseasonal to decadal scale. In Section 1, we will introduce the EISCAT radars and the experiments used. In Section 2, we will provide specific detail of how we have generated the archives, paying particular attention to the treatment of the data. Initial climatology's and comparisons to an empirical ionospheric model are presented in Section 3, with discussion and conclusions given in Sections 4 and 5, respectively.

1 EUROPEAN INCOHERENT SCATTER (EISCAT) RADARS

Ionospheric measurements have been made by the EISCAT radars in northern Norway since 1981 (Folkestad, Hagfors & Westerlund 1983; Baron 1986). The data presented here come from the UHF (ultra-high frequency) and VHF (very-high frequency) radars, which are both situated in Ramfjordmoen, near Tromsø, in northern Norway (69.58°, 19.23°, geographic coordinates). For a detailed description of the basis of the EISCAT radars see Rishbeth & Williams (1985), here we outline the important operational considerations.

The radars were operated on behalf of the scientific community by the EISCAT scientific Association, which is currently primarily funded by agencies in six Associate countries (Norway, Sweden, Finland, Japan, China, and the United Kingdom); past Associated countries have included France and Germany.

The UHF consists of a fully steerable, 32-m parabolic dish and operates at frequencies close to 930 MHz, with a peak power of 2 MW.

The 3 MW VHF radar is a 40 by 120 m parabolic trough with an elevation range of 15–90° and an operating frequency of 224 MHz. The trough dish consists of four individual panels that could allow for simultaneous different look directions, but in recent years has been limited to a single beam. The VHF frequency is better suited to measuring lower density plasmas, such as one might find in the D-Layer or topside of the ionosphere.

Until 2012 the UHF measured tristatic parameters at a designated altitude using two remote sites in Finland and Sweden; this capability was transferred to the VHF radar, due to noise interference from outside sources, and ceased completely in 2023.

Analysis of the returned radar signal allows recovery of standard ionospheric parameters such as electron density and temperature, ion temperature and ion velocity along the line of sight. Depending on the radar pulse code that is used, and the density of the ionosphere, these parameters can be obtained from altitudes above ∼60 km to heights in the topside ionosphere (∼2000 km).

The EISCAT radars do not run continuously, operating with a target of 1600 h yr^{-1} (depending on energy costs). This time is split evenly between user defined Special Programmes (SP) and standard Common Programmes (CP). CP time consists of six experiments, each targeted at different modes of operation using standardized scan patterns and pulse codes. These are synoptic observations, intended to build up an archive of measurements, which in recent years have also included the World Day campaigns, where all incoherent scatter radars in the world operate simultaneously.

The standard common experiments include; CP1, a field aligned experiment, providing good time resolution for auroral or substorm processes but also capable of running for longer time-scales, suitable for measurements of atmospheric tides, seasonal and solar-cycle variations; CP2 is a three or four-point scan (for example with the first three covering a triangle with vertical, south and south east and the fourth is field aligned) designed to measure wave-like phenomena; CP3 is a 17 position scan covering 10° in latitude in a 30 min cycle aimed at mapping parameters over a broad swathe of the ionosphere; CP4 is a low elevation scan suitable for observing high latitude plasma convection or polar cap phenomena; CP6 is a vertical D-region experiment designed to measure mesospheric heights, and lastly CP7 is a top-side vertical experiment probing high altitudes designed to study polar winds.

SP time consists of user defined experiments; these can include unusual pointing directions and pulse codes (sometimes non-incoherent scatter modes); though often use standard examples of both. Each Associate country has SP time to run each year and the data is then restricted to the user for a year before being made available for all associates.

2 ARCHIVE GENERATION

We have produced 20-yr archives of electron density measurements, at 1 h and 10 min integration times, by reanalysing measurements from the EISCAT UHF and VHF radars between 2001 and 2021. We are specifically looking at altitudes 50–200 km to capture the variability in the MLT-I region. To do this we have used the Grand Unified Incoherent Scatter Design and Analysis Package (GUISDAP) software (Lehtinen & Huuskonen 1996). GUISDAP fits autocorrelation functions to the measurements to produce standard ISR parameters, such as electron density. This is carried out for each altitude step. GUISDAP also provides power profile data, for some experiments, which is essentially electron density uncorrected for the difference in ion and electron temperature (valid for low altitudes where $T_i = T_e$, which we check for and will discuss in Section 2.4).

Fig. 1 demonstrates the data availability from UHF high elevation experiments for each month between 2001 and 2021, showing a reasonable spread of data throughout the seasons. Generally we have the lowest amount of data points during the spring months and throughout summer which we will have to account for when using these data for future analysis. Fig. 2 shows the same for the VHF radar, we have included a lot less data from the VHF radar primarily due to it often running at low elevations, which are excluded from our archives.

2.1 Data usage and preparation

We include all data from high elevation experiments ($> 60°$) between 2001 and 2021, including scanning modes as these data are intended for comparison with atmospheric models with much lower resolution grids and hence we do not need the fine-scale resolution. Table 1 details the EISCAT experiments that are included in this archive; most of which have been run in common program mode (we have only included data from CP1, CP2, CP6, and CP7, not CP3 or CP4 as these include low elevation scans.). These experiments differ in range coverage and resolution in range, time, and spectra. We are

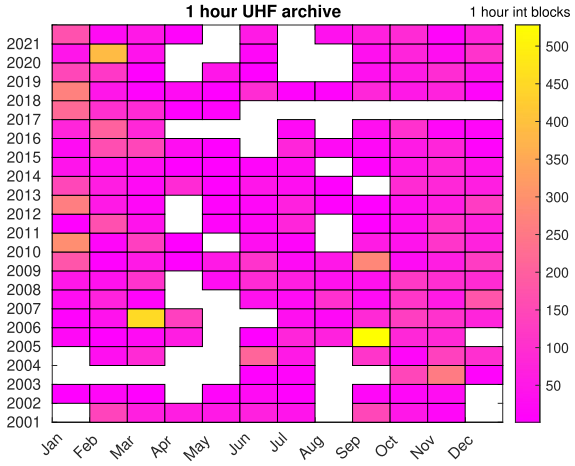

Figure 1. Data availability from the 1 h archive for the UHF radar (will be very similar for the 10 min archive).

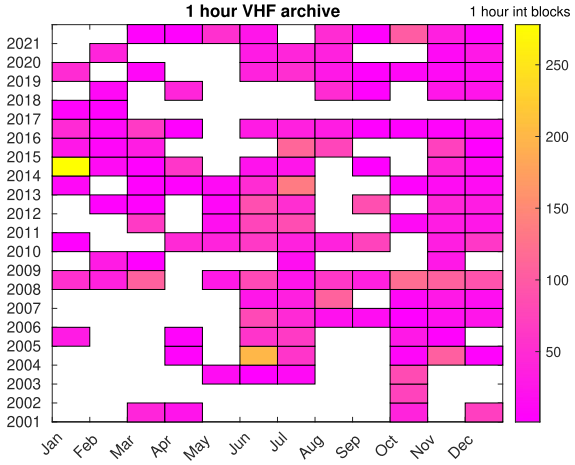

Figure 2. Data availability from the 1 h archive for the VHF radar (will be very similar for the 10 min archive).

Table 1. Experiment details for the different VHF/UHF experiments taken from Tjulin (2024).

	Range (km)	Range gate (km)	UHF	VHF	CP-type
arc1	95–420	0.9	yes	no	CP1
arc_d	60–139	0.3	yes	yes	CP6
beata	49–693	2.2	yes	yes	CP1, CP2
bella	47–1425	3.2	yes	yes	CP3, Cp4
cp1l	46–721	1.0/1.5	yes	no	CP1/2
cp7h	316–2400	2.25	no	yes	CP7
manda	19–209	0.36	yes	yes	CP6
tau1	104–2061	1.8/ 3.6	yes	yes	CP4
tau2pl	50–705	0.3	yes	no	CP1/2
tau8	52–1307	2.6	no	yes	CP4
tau7	78–2057	1.8	no	yes	CP7

not concerned with spatial ambiguity of including data at elevation angles down to $> 60^\circ$ as the UHF spends less than 1 per cent and 0.5 per cent of the time at these slightly lower elevations. The range gates listed in Table 1 are typically the highest spatial resolution for each experiment, however for some individual cases we had to increase this range gate or standardize to 3 or 3.5 km for the GUIDSAP analysis to run. We note that some experiments do not start/end on the hour for a multitude of reasons including scheduling so for subsequent analysis we require the integration time to be more than 40 min to be included in the 1-h archive and more than 7 min to be included in the 10-min archive.

When combining data from multiple experiments there are some important considerations. In preparing the data, we are aware of potential 'dangers' or sources of contamination such as Polar Mesospheric Summer and Winter Echos (PMSE/PMWE), which result in 'false' electron density signatures (discussed more in Section 2.5). Another key consideration is the EISCAT Heating facility. There is a High Frequency (HF) facility located at the radar site used for experiments to modify the natural plasma environment of the ionosphere (Rietveld et al. 1993); it has also been used as a diagnostic tool for studying the underlying mechanisms that produce PMSE (Chilson et al. 2000) and PMWE (Kavanagh et al. 2006). Thus, care must be taken when interpreting signatures in the EISCAT data such that they are not caused (or contaminated with) heating effects. There is a record of when the Heating facility (https://portal.eiscat.se/heating_logs/) is operated but this is not easily accessed for bulk data operations such as the construction of these archives; therefore, at this juncture we have not filtered for Heating experiments.

In practice it is unlikely that Heating experiments will have much affect on the electron density at the relevant altitude ranges, since many of the experiments were focused on the F-layer (for example, Rexer et al. 2021). Where the Heating experiments were used to modulate PMSE and PMWE, the natural signatures themselves are a greater problem. Consideration of the impact of heating on the data will be a feature of the analysis of the archive for specific studies in the future, especially those that consider the variability in electron and ion temperatures.

2.2 Importance of calibration

EISCAT data require calibration and historically this has been achieved in one of two ways: use of a plasma line measurement (Kirkwood, Collis & Schmidt 1986), or comparison of the peak critical frequency of the E (foE) and/or F (foF2) layers with a local Dynasonde (Rietveld et al. 2008). The comparison results in a 'magic constant', i.e. calibration number, that can be used to re-analyse the data to give a more accurate estimate of the ionospheric parameters. Studies have shown the electron density measurements are sensitive to cold and snow in the antennas of the radar, underestimating by a factor of 2 at times (Rietveld, Isham & Häggström 2005). When producing these archives, we have taken particular care to use the suggested magic constant listed in the calibration tables (https://eiscat.se/scientist/data/tromso-calibration-tables/). Where these were not available we went back through the schedule list and manually collected the relevant calibration numbers (https://portal.eiscat.se/schedule). Where more than one magic constant were available we show preference to foF2, then plasma line, then foE, except for the lower altitude experiments such as arc1, arcd, and manda where we generally showed preference to foE.

Fig. 3 shows electron density at an altitude of 120 km analysed using different calibration values. An order of magnitude difference, outside the errors of the measurement, in the electron density can be seen where we have used a magic constant value of 0.5 (bottom line) and 4 (top line), examples of typical low and high calibration values. As the calibration is clearly having a marked effect on the electron density, we have only included data in our archive where

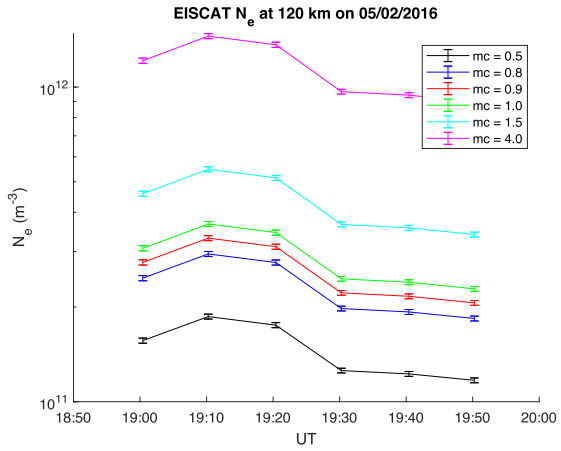

Figure 3. Figure showing electron density's produced by GUISDAP on 2016 February 5 using different calibration numbers.

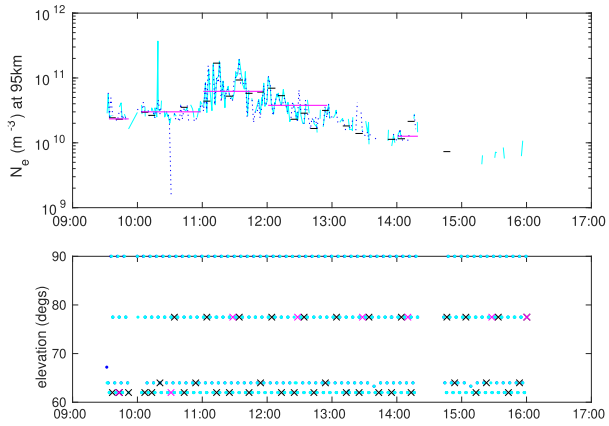

Figure 4. Top panel showing electron density at 95 km on 2014 November 22 beata CP2 experiment for 1 min integration (rapidly varying cyan line), scan resolution (blue dotted), 10 min integration (short horizontal black) and 1 h integration (long horizontal magenta). The bottom panel gives the radar elevation saved by GUISDAP corresponding to the same colours outlined above.

the calibration numbers were provided in calibration tables or in the schedule.

2.3 Validation of scanning experiments (CP2)

As we are currently including scanning experiments in the archive, we have taken a closer look at a CP2 experiment analysed over different integration times. Fig. 4 gives electron density at 95 km (top panel) and antenna elevation angle (bottom panel) during a CP2 experiment between 09:30-16 UT on 2014 November 22. The 1 min (highly varying cyan) and antenna scan time (blue dotted) data are fairly similar except a large deviation around 10:15 UT for the 1 min integration and at 10:30 UT for the antenna scan time, this is possibly a rogue value and does not seem to affect the 1 h integration value (magenta). However, there is no value for the 10 min integration value (short horizontal black) at this time, which could be affected by the rogue value. The 1 h, and most of the 10 min data, appear to be reasonable averages of the higher temporal data over their integration periods, for the first part of the interval before the data becomes sparse. We note, only three 'blocks' of 1 h data from this experiment would currently be included in our analysis of the archive due to our requirements of the integration to be made up of data from more than 40 min and the elevation of the radar to be greater than 60°.

The bottom panel of Fig. 4 shows the changes in radar elevation recorded for each integration period, demonstrating that we need to be careful of the values for the elevation from the scanning experiments as the 10 min and 1 h data blocks will be made up of data from multiple scan positions but the elevation value given by GUISDAP will not reflect this.

2.4 Inclusion of power profile data

Where available, we have included the 'raw' electron density (N_r) at the bottom of the fitted electron density (N_e) altitude profiles where the GUISDAP analysis has returned NaNs. The N_r values are essentially back-scatter power profiles measured by the radars at zero lag [the EISCAT data are stored as lag profiles (Virtanen et al. 2008)]. We use the assumption that $N_r = N_e$ where T_i/T_e is equal to unity [see fig. 9 of Semeter & Kamalabadi (2005)]; we smoothed the T_i/T_e altitude profiles using a Savitzky-Golay filter (Savitzky & Golay 1964), to identify the point where the ratio deviated from 1±0.1. Savitzky-Golay uses convolution, fitting (via linear least square) successive subsets of adjacent data points (within the 'frame') with a low degree polynomial (defined by the order) to smooth the data; we have used an order of 2 fit and a frame rate typically between 3 and 7, depending on the altitude resolution of the experiment. If more than one power profile were available for one integration period, a mean of the N_r at each altitude was taken. The raw electron density is available as a data product as part of this paper with the assumptions included up to now.

Before including the power profile in the analysis presented in this paper, we have filtered for the effects of negative ions on the low altitude raw electron density and corrected for the Debye length. We have not applied these filters to the published archive sample to allow future users to develop their own methods for dealing with these issues given the choices for limits can be somewhat objective and improved methods may arise.

Turunen (1993) reported that the existence of negative ions has considerable effect on the received signal power and subsequently the raw electron density profiles from EISCAT. The density of negative ions increases significantly in darkness below 80 km (Verronen et al. 2006). To remove the impact of these ions we have applied a simple filter below 80 km to exclude any power profile data when the solar zenith angle is above 90°.

Another factor to consider is as the electron density decreases, the Debye length becomes more important. In the fitted data from GUISDAP, this effect is accounted for; however, for the power profile data we either need to correct for the Debye lengths or filter out affected densities. Wickwar (1974) gives the following equation for the N_e:

$$N_e = N_r \frac{\left(1+\alpha^2+T_r\right)\left(1+\alpha^2\right)}{2}, \tag{1}$$

where T_r is the ratio of the ion and electron temperatures, assumed to be 1 as discussed above and the Debye length is accounted for in the α^2 term as follows (λ is the wavelength of the radar signal):

$$\alpha^2 = \left[\frac{4\pi D}{\lambda}\right]^2. \tag{2}$$

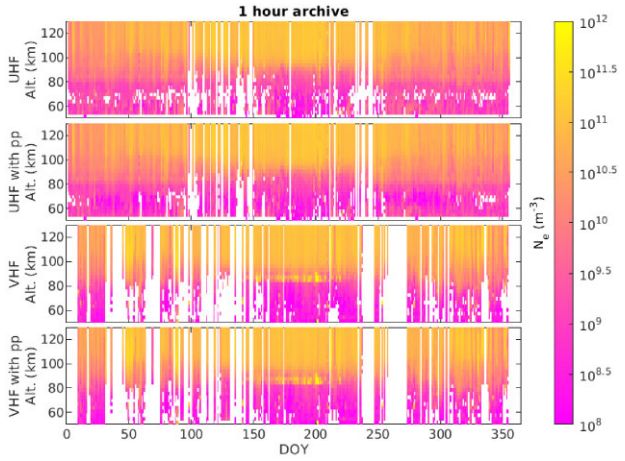

Figure 5. Figure showing a DOY climatology for the 1 h archive from the UHF radar without (a) and with (b) raw electron density data, and the VHF radar without (c) and with (d) raw electron density data.

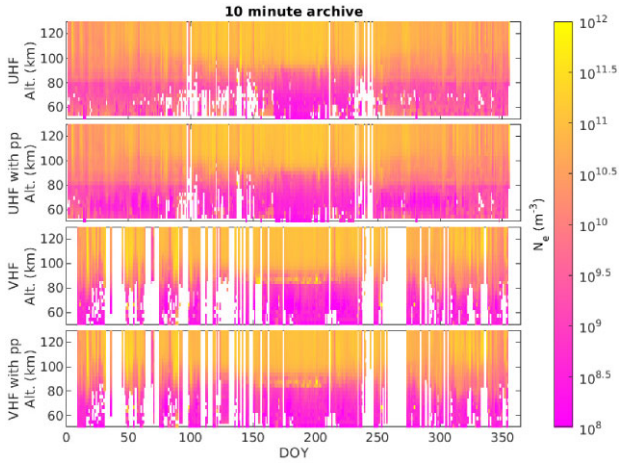

Figure 6. Same format as Fig. 5 for the 10 min archive.

We have retained the values of the raw electron density in our analysis if the value of the alpha term (the fraction in equation 1) is 0.01, i.e. it will change the value of the electron density by less than 1 per cent. These values of the raw electron density are included at the bottom of the electron density altitude profiles, where there are no data from the fitted electron density.

Figs 5(a) and (c) show a day of year (DOY) climatology of the 1 h archive between 2001 and 2021 for the UHF and VHF N_e measurements, respectively, Figs 5(b) and (d) show the same climatology with the N_r included. Fig. 6 shows the same for the 10 min archive; for both climatologies we are using the median electron density at each altitude for DOY. Here we have standardized the data between 50 and 200 km at 3 km altitude bins (although only shown to 120 km). The supplementary materials show these data split by experiment, demonstrating the majority of the UHF data coming from beata experiments and the majority of VHF data are from manda experiments.

One important feature seen in Figs 5 and 6 are the enhanced electron density that can be seen between ∼80 and 90 km over the summer months (DOY 150–250); these are not true electron density measurements but rather coherent scatter associated with noctilucent clouds, known as Polar Mesospheric Summer Echos

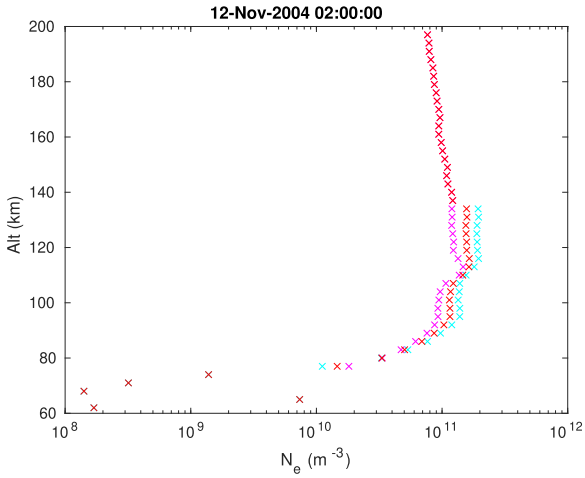

Figure 7. Figure showing UHF tau2pl (magenta), VHF arcd (cyan) for 2004 November 12 02–03 UT, the red crosses show the averaged of the two electron density profiles we will use in our combined archive.

(PMSE) (Ecklund & Balsley 1981). These figures highlight that PMSE are more visible in the VHF than the UHF data, this is due to the frequency of the radar, with PMSE being more visible at lower frequency ranges (Li & Rapp 2011).

Another feature to point out, which is particularly apparent in the UHF 10-min data (top panel of Fig. 6), is an increase in electron density around 60 km; this is an artefact likely due to a positive bias in the data due to the noise at the lower altitudes where there is lower electron density. When the power profile data are added this artefact is lessened but still something to be aware of, particularly in the winter months.

The second and fourth panels of Figs 5 and 6 demonstrate the benefit of using the raw electron density to fill in the gaps from the fitted measurements at lower altitudes, which is crucial for a study of the mesosphere. However there a few caveats we need to consider, particularly for the VHF 1 h data. Supplementary Figs S3 and S4, demonstrate that inclusion of the power profiles for the manda experiments has added a lot of noise to the lower altitudes (also seen to a lesser extent in the UHF manda experiments in supplementary Fig. S2). The power profile derived from manda on the VHF tends to be noisy as it comes from only half of the receiver and the code does not provide a true zero lag estimate. Thus we do not include it. Alternating codes do not provide any true zero-lag, so the power profile is taken at a short offset from the zero-lag. Furthermore, the power profile data do not go through as rigorous analysis routines as the fitted data from GUISDAP, therefore the raw data are more susceptible to contamination due to meteors and PMSE, particularly in the VHF data (Brosch et al. 2010) and when integrating over longer periods. Continuing forward with our analysis in this paper, we do not use manda power profile data and are cautious with the 1 h data at the lower altitudes.

2.5 Combining VHF and UHF data

When the UHF and VHF were running at the same time, we have averaged the data at each altitude in our region of interest (50–120 km). Fig. 7 shows the UHF (magenta), VHF (cyan), and averaged data (red) on 2004 November 12 for the integration period 02–03 UT, during this period the UHF and VHF radars were running tau2pl and arcd experiments, respectively.

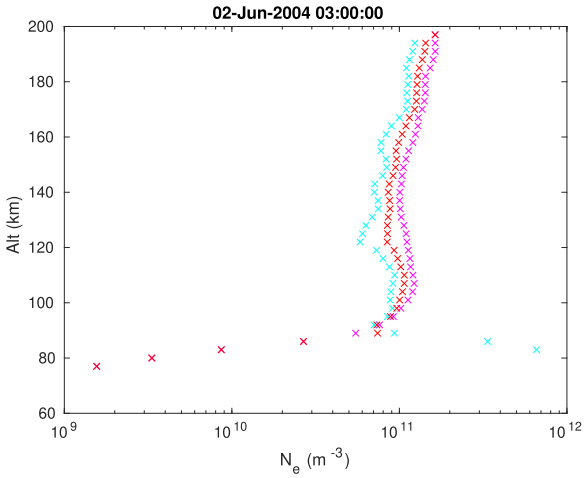

Figure 8. Figure demonstrating an altitude profiles from a period where both radars were running simultaneously when a PMSE signature is visible in the VHF tau8 data (cyan) but not the UHF tau2pl data (magenta); the combined average profile (red) only uses data from the UHF in the altitudes of the suspected PMSE signature.

We have performed an initial simplified method to remove the effects of PMSE when combining the data sets from the different radars. In instances where data from both the VHF and UHF were available for altitude bins between 80 and 90 km, if the VHF data were more than an order of magnitude greater than the UHF data, we ignored the VHF data and used the UHF data. If we just had VHF data, we looked at ±2 altitude bins for the data between 80 and 90 km, and if there were an order of magnitude jump in these data, the data were not included. We are not currently addressing the effect of Polar Mesospheric Winter Echos (PMWE) in this archive as they are not as apparent, though we note they could have an effect during winter and equinox months between 55 and 85 km (Strelnikova & Rapp 2013).

Fig. 8 gives an example from 2004 June 2, between 03 and 04 UT, where a large spike in the VHF data is visible between 80 and 90 km, likely due to PMSE; at this time the VHF (cyan) was running a tau8 experiment and the UHF radar (magenta) was running a tau2pl experiment. The averaged-combined data, shown in red, only uses the UHF data between the altitudes of the suspected PMSE.

Figs 7 and 8 illustrate that despite running at the same time, the UHF and VHF measure slightly different values for the electron density. There are potentially a number of different reasons for this; the radar will be sampling the ionosphere with some small separation in space and natural ionospheric variability could result in a different electron density value. It is also important to note that in the case of CP1 field aligned experiment, the measurement is along a magnetic flux tube, while for a CP2 experiment (60–90-degree elevation), the measurement is cut across different flux tubes at different altitudes, meaning the radars are measuring slightly different ionosphere. The calibration numbers for each radar were during both examples were somewhat different, i.e on the 2004 November 12 (Fig. 7), the calibration number used for the UHF analysis was 1.00 and VHF was 2.25; for the 2004 June 4 example, the UHF analysis used a calibration number of 1.27 and the VHF analysis used 1.34.

The 'magic constant'/ calibration number effectively scales the electron density in the analysis (as described in Section 2.2) and differences from experiment to experiment (and radar to radar) arise due to small changes in the radar systems and other external factors that affect the received power, such as snow collection in the dish.

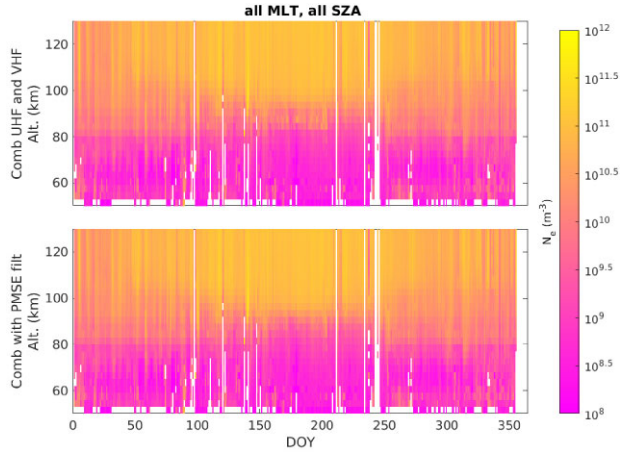

Figure 9. DOY climatology made up of data from both the UHF and VHF radars.

The differences here would likely point to mechanical influences on the received power as well as any potential differences in the overhead ionosphere.

Fig. 9 shows the DOY climatology for the combined UHF and VHF data for the 10 min archive, the top panel is all the data and the bottom panel shows the data with the simple PMSE-filter described above. These data, which we will use in our analysis for the rest of the paper, do not include the manda power profile data (as discussed in Section 2.4) and have a noise threshold of ±5 standard deviations from the mean applied at each 3 km altitude bin. The PMSE signature in the combined data (top panel of Fig. 9) is less obvious than in VHF data (the bottom panels of Fig. 6) but still visible. Furthermore, the PMSE-filtered version (bottom panel of Fig. 9) are suggestive of a potential UHF depletion of electron density, sometimes referred to as a 'bite out' at PMSE altitudes in UHF data (e.g. Li & Rapp 2013); therefore care must be taken when using data from the summer months at PMSE altitudes. Performing a more rigorous PMSE filter is a large volume of work not in the scope of this paper and therefore we leave for future studies.

3 INITIAL RESULTS

3.1 Comparison with an empirical model

Fig. 10 shows a comparison of DOY climatologies from the combined UHF-VHF 10-min archive (top panel, same as Fig. 9), with the Empirical Canadian High Arctic Ionospheric Model (E-CHAIM) (Themens et al. 2017) (second panel) between 2001 and 2021. The third panel of Fig. 10 shows the difference between the two climatology's and the fourth panel gives the number of data points at each DOY. E-CHAIM has been run over the same time periods as the EISCAT experiments and we note the DOY climatology for the 1-h archive, not shown, gave similar results. To provide the most representative comparison with the EISCAT data we ran E-CHAIM with the NmF2 perturbation model, described in Themens et al. (2017), to accommodate the change in ionospheric density during geomagnetic storms and the precipitation module to account for auroral precipitation in the E-region (Watson, Themens & Jayachandran 2021). We also included the D-region chemistry that was incorporated into E-CHAIM through the integration of the Faraday-IRI-2018 model (Friedrich, Pock & Torkar 2018).

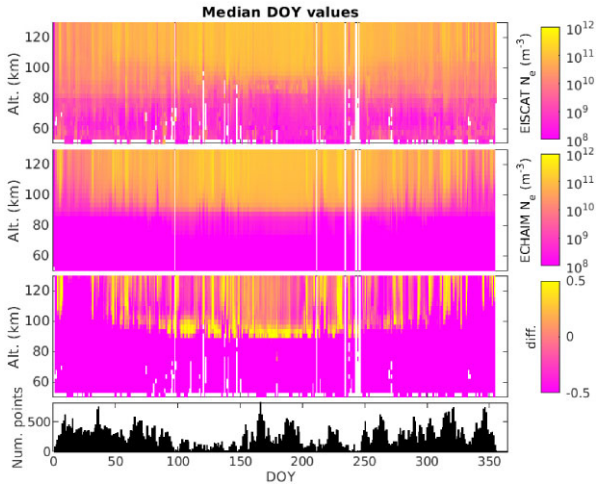

Figure 10. Top panel showing the DOY climatology for the EISCAT 10 min archive, second panel showing E-CHAIM data run at the same time we have EISCAT data, third panel giving the difference between the two ((model-data)/data).

Fig. 10 illustrates the seasonal variability of the electron density in both EISCAT and E-CHAIM. The E-CHAIM N_e is maximum and extends to the lowest altitudes in the summer months and decreases in the winter months, the effect is due to the solar irradiance changing with the season and is quite pronounced due to the high geographic latitude of the radars, located in Tromsø, Norway. The EISCAT N_e shows a similar summer enhancement but has the lowest altitude enhancements in the winter months. This is likely due to E-CHAIM's precipitation model only accounting for lower energy auroral precipitation and not the medium and higher energy precipitation from the radiation belts and plasmasheet.

The third panel of Fig. 10 gives the difference between the model and the data, with the pink (darker shade) values representing where the EISCAT N_e is higher than the model and the yellow (lighter shade) showing the opposite; in general, E-CHAIM is underestimating the electron density measured by EISCAT, except at higher altitudes where there are differences in the variability. There's an interesting enhancement in E-CHAIM data between 80 and 90 km starting around DOY 80 and lasting most of the summer months up to around DOY 200. This is around PMSE altitudes, however the PMSE signatures in EISCAT appear around DOY 150. This feature could be due to the inclusion of the D-region data in E-CHAIM, which transitions to use the FIRI model (Friedrich et al. 2018) around these altitudes. E-CHAIM uses a sigmoid function to transition from its normal E-Region to the FIRI D-Region model, so there is pass-off point where you go from one model to the other. In some cases, the altitude of FIRI's E-Region is rather far below E-CHAIM's; when this occurs the electron density will decrease below the E-CHAIM E-Region peak, but then increase again as it transitions to FIRI which can lead to a slight bump in electron density on the bottom of the E-Region.

3.2 Seasonal variability

Fig. 11 shows the magnetic local time variation of electron density in the 1 h archive split by season (Winter = Nov-Feb, Equinox = March-Apr, Sept-Oct, Summer = May-August). A clear seasonal effect, from the UV ionization can be seen with the summer months having higher electron density around midday than in winter; the winter seasons (top panel) show the effects of electron precipitation which peaks around magnetic midnight at 100 km, as expected for auroral precipitation enhancing the E-layer.

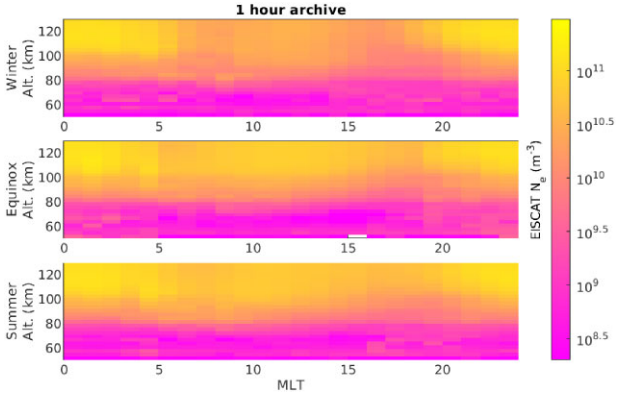

Figure 11. Magnetic local time climatology for the 1 h electron density archive, split by season.

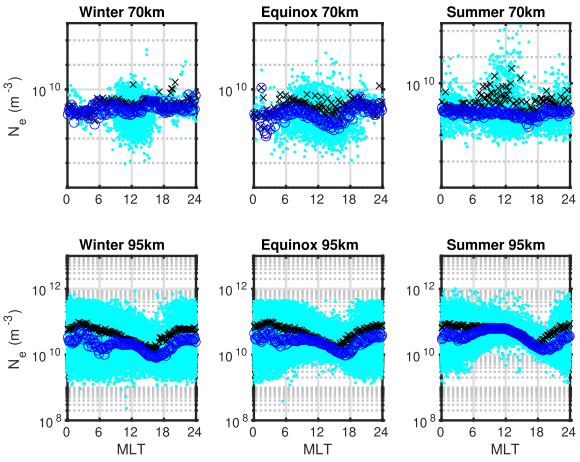

Figure 12. Figure showing the variability in electron density (N_e) for the 10 min archive at 70 and 95 km, separated by season. The mean value for each hour is indicated by a black cross and the median is indicated by a dark blue circle.

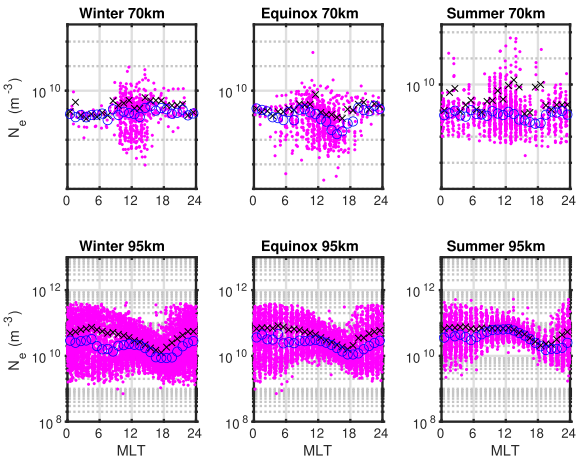

Figure 13. Same format as Fig. 12 but for the 1 h archive.

Figs 12 and 13 show the electron density variation at 70 km (top row) and 95 km (bottom row), split by season, for the 10 min and 1 h

archives, respectively. The black crosses give the mean value and the blue circles the median for each 10 min/1 h intervals throughout the day in each season, with all the data shown in cyan dots and magenta dots for the 10 min and 1 h archives, respectively; these altitudes were chosen to mitigate the effects from the PMSE.

A pattern emerges at 95 km for all seasons in both the 1 h and 10 min archive where a peak in the morning MLT sector (dawn-sector), a minimum in the afternoon (dusk-sector) and an increase approaching midnight. This follows a similar pattern to that reported in Kavanagh et al. (2004) for auroral absorption from riometers representing precipitation into the E and D layers, and is what we expect from electron density enhanced by electron precipitation on the dawnside and substorm enhancements around midnight and as discussed above for Fig. 11. In summer and equinox, the minima occur at a later magnetic local time, due to the effect of solar illumination and for summer in particular, the morning/midday peak is more pronounced due to the increase in solar illumination. Around the magnetic local times affected by precipitation, where there are larger variations in the data, the mean and median show quite different values as the mean is more sensitive to outliers but during the daytime where there is less variation, the mean and median show consistent results.

At 70 km (top row of Figs 12 and 13), the electron density is lower than at 95 km, as expected, and approaching the noise floor of EISCAT and hence we need to be careful with interpreting these data; however, with the 10 min and 1 h integration times we have improved our signal-to-noise ratio and hopefully lessened the effect of noise on our data. During the summer months there is a peak around midday which is likely due to effect of solar illumination creating ionization at lower altitudes. During equinox, a similar pattern can be seen as for the 95 km plots below where there is a minima around 14/15 MLT and the hint of a peak can be seen between 7 and 8 MLT, clearest for the 10 min archive (Fig. 12); we speculate this pattern could be due to the higher energy precipitation from the radiation belts penetrating to the lower altitudes (Lam et al. 2010). A secondary peak in N_e can be seen around between 18 MLT and midnight, in the 'substorm' region, is also present.

4 DISCUSSION

The longevity of the EISCAT radars provide a nearly unique source of data for probing the high latitude, auroral ionosphere across multiple time-scales. The long-term observations provide an opportunity to examine the ionospheric response to driving from various space weather processes and from changes in the lower atmosphere conditions. The archives detailed in this paper were specifically compiled to examine the variations in the ionosphere that overlaps the mesosphere – lower thermosphere in response to driving from multiple processes in the sub-seasonal to decadal range (e.g. stratospheric warmings, large-scale planetary waves, the north Atlantic oscillation, solar cycle variations, etc). However, the data will be available for studies determined by other users in the future.

Compiling the archives required overcoming several significant challenges; the EISCAT radars have run on various experiments over the years employing varying look directions, scan patterns and pulse codes. When combining data from the two co-located radars (the UHF and VHF), we took a mean of the electron density measurements when the radars were running simultaneously and for the PMSE-filtered version, only used UHF data between 80 and 90 km during suspected PMSE contamination. The data needed to be selected with care and analysis of the raw data, significant thought went into the appropriate calibration to provide the best estimates of the ionospheric parameters. This was a major challenge (see Section 2.2); the calibration number scales the electron density measurement during the analysis process (see Fig. 3) and the number selected often relied on the experiment that was being carried out. Where a calibration number was not available, we have not included the corresponding data.

Any measurement of the ionosphere using the incoherent scatter technique is essentially an estimate based upon the fitting process to the observed spectrum. However, even when the same analysis is used some variation appears: Figs 7 and 8 show that the UHF and VHF can produce differences when measuring the same ionosphere. As discussed in Section 2.5, this can be partially explained due to the differences in the radar systems as illustrated in the different calibration constants. This highlights the need for good estimates of the calibration.

A fundamental difference in the UHF and VHF data are the presence of PMSE. Fig. 6 highlights that the VHF radar is more sensitive to PMSE, this is due to the frequency it operates (e.g. Li & Rapp 2013). We have demonstrated a simple approach to removing PMSE described in Section 2.5 but leave a more rigorous attempt for future work. We have not addressed the PMWE in this paper as the signature is not as dominant as the PMSE. The published archive has no filtering for either PMSE or PMWE and thus users must show caution for the electron densities at affected altitudes (between 80 and 90 km for PMSE in the summer months and between 55 and 85 km for PMWE during the winter).

The VHF data are also slightly more sensitive to contamination due to meteors (Brosch et al. 2010). Meteors are very well resolved in the fitted spectral data from GUISDAP but the power profile data (raw electron density described in Section 2.4) are known to be nosier as the meteors are not resolved. This is clear from panels 3 and 4 of Figs 5 and 6, with the 1 h data suffering more from the contamination due to the longer integration period. The power profile data from manda, a D-region experiment, are excluded from our analysis as the experiment is higher resolution and uses smaller range gates and is hence more susceptible to meteor contamination.

A final factor to be aware of when using the archives are heating experiments, full descriptions of when heating was operating are not readily available (there is some indication in the MADRIGAL archive) and as such some careful checking is required when using the data archives. As stated earlier the primary use of these data is for investigating the lower ionosphere, well below the main effects of many heating experiments. It is well established that the operation of heating has a direct impact on the recorded transmit power of the radar and this will be used in future studies to discriminate period of heating operations as and when required. It is worth noting that heating experiments have been carried out on the D-layer, but mostly with the aim of modulating and probing PMSE and PMWE, which, as stated, are a potentially larger source of contamination to the electron density and need to be considered carefully.

We have investigated the seasonal dependence of electron density as a function of the magnetic local time and altitude in Fig. 11 and then demonstrated the variability of these measurements at 70 and 95 km in Figs 12 and 13 (these altitudes were chosen to avoid contamination from PMSE). Fig. 14 compares the median values from both the 10-min (cyan crosses) and 1-h (magenta circles) archive.

At 95 km, we see a pattern consistent with what we expect for the electron precipitation during winter and equinox in different MLT sectors (Kavanagh et al. 2004, 2006), with the strongest precipitation around dawn and midnight, and a minima in the afternoon when the radars are in the typically 'quiet' dusk sector. During summer we see a pattern dominated by solar illumination during the day times, with

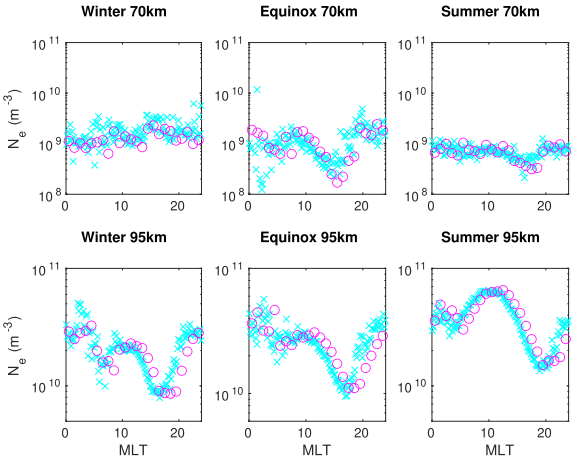

Figure 14. Figure showing the median values seasonal N_e values by magnetic local time for the 10 min (cyan crosses) and 1 h (magenta circles) archives.

smaller peaks around midnight due to the precipitation. At 70 km, we see a peak in between around 08–12 MLT, clearest during the equinox months. We propose this is due to the medium and high energy electron precipitation from the radiation belts, scattered by chorus (which are present in these MLT-sectors; Meredith et al. 2003), typically reaching lower altitudes than auroral precipitation, although we note the densities are very low at this altitude and potentially near the noise floor. Figs 12 and 13 highlight the variability in the electron density measurements at 10 min (cyan dots) and 1 h (magenta dots), respectively; this demonstrates why we need to think carefully presenting average values using the mean and median, with the mean values tending to be more susceptible to density variations.

Fig. 10 illustrates that the highly variable nature of the electron density measurements are not being reproduced in the E-CHAIM data below 100 km. This is partially due to the medium and high energy precipitation not yet being included in E-CHAIM. These archives will be integral in future work for investigating and quantifying the key sources of variability in the MLT-I region and feeding that back to the atmospheric modelling community to improve atmospheric models.

5 CONCLUSION

We have produced two archives of EISCAT mainland data from both the UHF and VHF, from 2001 to 2021, integrated at 10 min and 1 h between 50 and 200 km with different range gates depending on the experiment. This is the first time data from the UHF and VHF have been combined in such a way to allow for longer term studies; this is something that has previously been difficult to do due to the non-continuous nature of EISCAT. When preparing these archives we have made several decisions to produce the most accurate representation of the ionospheric measurements for comparisons with atmospheric models who have much larger grid points than the EISCAT scan experiments (above 60°). The purpose of these archives is to look at variability in the mesosphere on different time-scales driven by both space weather and atmospheric processes. The underlying data presented in the analysis of this paper can be recreated using the tools described in Section 2 with the main aspects summarized as follows:

(i) We have only included data from above 60° elevation, including CP2 scanning experiments.

(ii) For the 1 h archive we require a minimum integration time of 40 min and for the 10 min archive we require a minimum integration time of 8 min.

(iii) When the UHF and VHF data were running simultaneously, we have taken the average of the two.

(iv) Where available (and not including manda experiments), we have included raw electron density measurements for altitudes below the fitted measurements.

The data published in the archive do not have these tools applied and therefore there is scope to regenerate the archives using different choices of merging, filtering, etc, as new techniques arise.

The key initial results we have from the development of these archives are as follows:

(i) Both archives highlight that PMSE signatures are much more apparent in VHF data compared to UHF data, a caveat to be aware of when using these data.

(ii) We have shown the magnetic local time dependence of electron density for both the 10-min and 1-h archives fits the average pattern expected for precipitation-driven variability at two different altitudes. The seasonal pattern also fits what is expected for the solar illumination dependence at high latitudes.

(iii) We have demonstrated the need for more finely tuned MLT-I models, with E-CHAIM not re-producing the variability seen in the EISCAT data, particularly at the lower altitudes.

ACKNOWLEDGEMENTS

We acknowledge the Rutherford Appleton Laboratory and the Natural Environment Research Council (NERC) supported UK EISCAT Support group (UKESG) for use of their computers and access to the raw EISCAT data they have stored, as well as software support when we were generating these new archives. JAR and AJK are supported by the NERC grant NE/V018426/1.

DATA AVAILABILITY

The 1 h and 10 min archives described in this paper are available at the Polar Data Center: Reidy, Kavanagh, and Wild (2025).

The source code for E-CHAIM in the C, Matlab, and IDL languages is currently openly available online at https://e-chaim.chain-project.net. This study uses version 3.3.0 of E-CHAIM. Infrastructure funding for CHAIN was provided by the Canadian Foundation for Innovation and the New Brunswick Innovation Foundation.

REFERENCES

Akmaev R. A., 2011, Rev. Geophys., 49, RG4004
Baron M., 1986, J. Atmos. Terr. Phys., 48, 767
Brosch N., Häggström I., Pellinen-Wannberg A., Westman A., 2010, MNRAS, 401, 1069
Chilson P. B., Belova E., Rietveld M. T., Kirkwood S., Hoppe U.-P., 2000, Geophys. Res. Lett., 27, 3801
Ecklund W. L., Balsley B. B., 1981, J. Geophys. Res., 86, 7775
Folkestad K., Hagfors T., Westerlund S., 1983, Radio Sci., 18, 867
Friedrich M., Pock C., Torkar K., 2018, J. Geophys. Res. (Space Physics), 123, 6737
Gimeno L., 2013, Front. Earth Sci., 1
Goncharenko L., Zhang S.-R., 2008, Geophys. Res. Lett., 35, L21103
Goncharenko L. P., Coster A. J., Chau J. L., Valladares C. E., 2010, J. Geophys. Res. (Space Physics), 115, A00G07
Kavanagh A. J., Kosch M., Honary F., Senior A., Marple S., Woodfield E., McCrea I., 2004, Ann. Geophys., 22, 877

Kavanagh A. J., Honary F., Rietveld M. T., Senior A., 2006, Geophys. Res. Lett., 33, L19801
Kavanagh A. J., Honary F., Donovan E. F., Ulich T., Denton M. H., 2012, J. Geophys. Res. (Space Physics), 117, A00L09
Kirkwood S., Collis P. N., Schmidt W., 1986, J. Atmos. Terr. Phys., 48, 773
Lam M. M., Horne R. B., Meredith N. P., Glauert S. A., Moffat-Griffin T., Green J. C., 2010, J. Geophys. Res. (Space Physics), 115, A00F08
Laštovička J., 2006, J. Atmos. Sol. Terr. Phys., 68, 479
Lehtinen M. S., Huuskonen A., 1996, J. Atmos. Terr. Phys., 58, 435
Li Q., Rapp M., 2011, J. Atmos. Sol. Terr. Phys., 73, 944
Li Q., Rapp M., 2013, J. Atmos. Sol. Terr. Phys., 104, 270
Meredith N. P., Horne R. B., Thorne R. M., Anderson R. R., 2003, Geophys. Res. Lett., 30, 7–1
Pedatella N. M., Liu H. L., 2018, Geophys. Res. Lett., 45, 4578
Reidy J., Kavanagh A., Wild M., 2025, Data from the EISCAT UHF and VHF between 2001–2021, integrated at 10 minutes and 1 hour between 50–200km (Version 1.0) [Data set], NERC EDS UK Polar Data Centre
Rexer T., Leyser T., Gustavsson B., Rietveld M., 2021, J. Geophys. Res. (Space Physics), 126, e29379
Rietveld M. T., Kohl H., Kopka H., Stubbe P., 1993, J. Atmos. Terr. Phys., 55, 577
Rietveld M., Isham B., Häggström I., 2005, EISCAT (European Incoherent Scatter) Scientific Association Report, 20071114. European Incoherent Scatter Scientific Association, Sweden
Rietveld M. T., Wright J. W., Zabotin N., Pitteway M. L. V., 2008, Polar Sci., 2, 55
Rishbeth H., Williams P. J. S., 1985, R. Astron. Soc. Quart. J., 26, 478
Savitzky A., Golay M. J. E., 1964, Anal. Chem., 36, 1627
Semeter J., Kamalabadi F., 2005, Radio Sci., 40, RS2006
Strelnikova I., Rapp M., 2013, Ann. Geophys., 31, 359
Themens D. R., Jayachandran P. T., Galkin I., Hall C., 2017, J. Geophys. Res. (Space Physics), 122, 9015
Tjulin A., 2024, EISCAT Experiments, 3 edn. European Incoherent Scatter Scientific Association, Sweden, available at: https://eiscat.se/wp-content/uploads/2024/12/Experiments.pdf
Turunen E., 1993, J. Atmos. Terr. Phys., 55, 767
Verronen P. T., Ulich T., Turunen E., Rodger C. J., 2006, Ann. Geophys., 24, 187
Virtanen I. I., Lehtinen M. S., Nygrén T., Orispää M., Vierinen J., 2008, Ann. Geophys., 26, 571
Watson C., Themens D. R., Jayachandran P. T., 2021, Space Weather, 19, e2021SW002779
Wickwar V. B., 1974, Analysis Techniques for Incoherent-Scatter Data, Interpretation in the 100–300 km Region, Report. Stanford Research Institute, Stanford

SUPPORTING INFORMATION

Supplementary data are available at *RASTAI* online.

supplementary.pdf

Please note: Oxford University Press is not responsible for the content or functionality of any supporting materials supplied by the authors. Any queries (other than missing material) should be directed to the corresponding author for the article.

This paper has been typeset from a TEX/LATEX file prepared by the author.